Twistronics of Kekulé Graphene: Honeycomb and Kagome Flat Bands

Michael G. Scheer and Biao Lian
Department of Physics, Princeton University, Princeton, New Jersey 08544, USA

(Received 15 June 2023; accepted 10 November 2023; published 26 December 2023)

Kekulé-O order in graphene, which has recently been realized experimentally, induces Dirac electron masses on the order of $m \sim 100$ meV. We show that twisted bilayer graphene in which one or both layers have Kekulé-O order exhibits nontrivial flat electronic bands on honeycomb and kagome lattices. When only one layer has Kekulé-O order, there is a parameter regime for which the lowest four bands at charge neutrality form an isolated two-orbital honeycomb lattice model with two flat bands. The bandwidths are minimal at a magic twist angle $\theta \approx 0.7°$ and Dirac mass $m \approx 100$ meV. When both layers have Kekulé-O order, there is a large parameter regime around $\theta \approx 1°$ and $m \gtrsim 100$ meV in which the lowest three valence and conduction bands at charge neutrality each realize isolated kagome lattice models with one flat band, while the next three valence and conduction bands are flat bands on triangular lattices. These flat band systems may provide a new platform for strongly correlated phases of matter.

DOI: 10.1103/PhysRevLett.131.266501

Introduction.—Moiré systems formed by twisting and stacking two-dimensional (2D) materials often exhibit flat electronic bands. The physics in flat bands is dominated by interactions, so strongly correlated phases often appear. A paradigmatic example is twisted bilayer graphene (TBG) at the magic angle $\theta \approx 1.05°$ [1], which hosts flat bands with fragile topology [2–5] and exhibits a variety of topological and interacting phases including correlated insulators, Chern insulators, and superconductors [6–13]. Similar flat band physics has been observed in moiré systems of multilayer graphene [14–16] and transition metal dichalcogenides [17–21].

An important class of flat bands consists of those arising in tight-binding models due to wave function interference effects [22–24]. Examples include the flat bands in the kagome lattice one-orbital and honeycomb lattice two-orbital tight-binding models [25,26]. Recently, we showed that such flat bands may be realized in moiré heterobilayers of graphene and certain 2D materials with lattice constant approximately $\sqrt{3}$ times that of graphene [27,28]. This motivates us to search for flat bands in the twistronics of *Kekulé graphene*, which is graphene with a $\sqrt{3} \times \sqrt{3}$ distortion. Kekulé graphene has been experimentally realized via epitaxial growth on a copper surface [29], lithium or calcium intercalation [30–32], or dilute lithium deposition [33,34]. Kekulé orders have also been observed in graphene in a magnetic field [35,36] and in correlated insulator phases of TBG [37].

In this Letter, we focus specifically on graphene with the Kekulé-O bond order illustrated in Fig. 1(a), which can be realized by intercalation or dilute deposition of lithium [32,34] and exhibits massive Dirac electrons at low

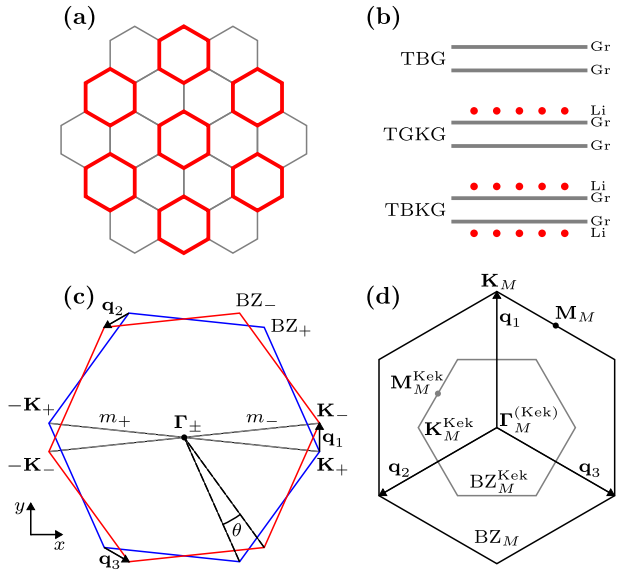

FIG. 1. (a) Kekulé-O bond order in graphene. The red and gray bonds indicate hoppings of different magnitudes between neighboring on-site carbon p_z orbitals. (b) TBG (top) and possible realizations of TGKG (middle) and TBKG (bottom) using intercalated or dilutely deposited lithium atoms (red) and graphene monolayers (gray). (c) The top ($l = +$) and bottom ($l = -$) layer graphene BZs before development of Kekulé-O order are labeled BZ$_l$. The Kekulé-O order induces Dirac masses m_l which couple the $\mathbf{K}_l$ and $-\mathbf{K}_l$ points, as indicated. (d) The larger hexagon labeled BZ$_M$ is the moiré BZ for TBG and TGKG. The smaller hexagon labeled BZ$_M^{\mathrm{Kek}}$ is the Kekulé moiré BZ for TBKG. The moiré $\mathbf{q}_j$ vectors [defined in panel (c)] and high symmetry momenta in both BZs are shown.

energy [33,38] (see Supplemental Material [39] Sec. II). We derive a continuum model for TBG with or without Kekulé-O distortions and study two cases: (i) twisted graphene on Kekulé-O graphene (TGKG), in which only one layer has a Kekulé-O distortion, and (ii) twisted bilayer Kekulé-O graphene (TBKG), in which both layers have Kekulé-O distortions. Possible realizations of these systems are illustrated in Fig. 1(b).

Despite the Kekulé-O distortion, the moiré unit cell of TGKG is the same as that of TBG. For twist angle θ near 1° and Dirac mass $m \lesssim 200$ meV in one layer, TGKG exhibits an isolated two-orbital honeycomb lattice flat band model at charge neutrality. In particular, there is a magic angle $\theta \approx 0.7°$ and Dirac mass $m \approx 100$ meV for which the second valence and conduction bands become extremely flat.

In the case of TBKG, the moiré unit cell is enlarged to a $\sqrt{3} \times \sqrt{3}$ supercell relative to TBG when both layers have nonzero Dirac mass. For twist angle θ near 1° and Dirac mass $m \gtrsim 100$ meV in both layers, the lowest valence and conduction bands in TBKG at charge neutrality are one-orbital kagome lattice flat bands, with bandwidths that generally decrease with increasing m and decreasing θ. The next two sets of connected valence and conduction bands in this regime are flat bands on triangular lattices.

Generic continuum model.—We consider a twisted bilayer moiré system in which each layer is either graphene or Kekulé-O graphene. We denote the top and bottom layers by $l = +$ and $l = -$, respectively. Layer l is rotated by angle $-l\theta/2$ relative to the aligned configuration, and the twist angle θ is small. We denote the lattice constant of layer l by a_l, and define the interlayer biaxial strain $\epsilon = \ln(a_-/a_+)$. The hexagonal Brillouin zone (BZ) of graphene layer l before the development of Kekulé-O order is shown in Fig. 1(c) and is denoted BZ_l.

The electrons at low energies in graphene layer l and valley $\eta = \pm$ without Kekulé-O order have a Dirac Hamiltonian $h_{l,\eta}(\mathbf{p}) = \hbar v_l(\eta\sigma_x p_x + \sigma_y p_y)$ at small momentum $\mathbf{p} = p_x\hat{\mathbf{x}} + p_y\hat{\mathbf{y}}$ measured from $\eta\mathbf{K}_l$, where the high symmetry momenta $\mathbf{K}_l = (4\pi/3a_l)R_{-l\theta/2}\hat{\mathbf{x}}$ are shown in Fig. 1(c). Here, v_l is the Fermi velocity of layer l, σ_0 is the 2×2 identity matrix, and σ_x, σ_y, and σ_z are the Pauli matrices. The Hamiltonian $h_{l,\eta}(\mathbf{p})$ is written in the graphene sublattice basis $\alpha = +$ and $\alpha = -$, which indicate sublattices A and B, respectively. We neglect spin degrees of freedom for simplicity.

A Kekulé-O order in layer l modifies the Fermi velocity v_l and induces an intervalley hopping term $m_l\sigma_x$ [33,38] (see Supplemental Material [39] Sec. II). This intervalley term produces a Dirac electron energy gap of $2m_l$, and we refer to m_l as the Dirac mass. Additionally, we consider a potential energy difference E_Δ between the two layers, which can arise from chemical dopants or an out-of-plane displacement field.

In the continuum (i.e., small $|\mathbf{p}|$) limit, we denote the real space basis for Dirac electrons at position $\mathbf{r}$ in layer l, valley η, and sublattice α by $|\mathbf{r}, l, \eta, \alpha\rangle$. The continuum Hamiltonian of this moiré system then takes the form $H = \int d^2\mathbf{r}|\mathbf{r}\rangle\mathcal{H}(\mathbf{r})\langle\mathbf{r}|$, where

$$\mathcal{H}(\mathbf{r}) = \begin{pmatrix} E_\Delta\sigma_0 - i\hbar v_+\boldsymbol{\sigma}\cdot\nabla & m_+\sigma_x & T(\mathbf{r}) & 0 \\ m_+\sigma_x & E_\Delta\sigma_0 + i\hbar v_+\boldsymbol{\sigma}^*\cdot\nabla & 0 & T^*(\mathbf{r}) \\ T^\dagger(\mathbf{r}) & 0 & -i\hbar v_-\boldsymbol{\sigma}\cdot\nabla & m_-\sigma_x \\ 0 & T^T(\mathbf{r}) & m_-\sigma_x & i\hbar v_-\boldsymbol{\sigma}^*\cdot\nabla \end{pmatrix}, \tag{1}$$

we have defined the basis row vector

$$|\mathbf{r}\rangle = \big(|\mathbf{r},+,+,+\rangle\,|\mathbf{r},+,+,-\rangle\,|\mathbf{r},+,-,+\rangle\,|\mathbf{r},+,-,-\rangle\,|\mathbf{r},-,+,+\rangle\,|\mathbf{r},-,+,-\rangle\,|\mathbf{r},-,-,+\rangle\,|\mathbf{r},-,-,-\rangle\big), \tag{2}$$

and $\boldsymbol{\sigma} = \sigma_x\hat{\mathbf{x}} + \sigma_y\hat{\mathbf{y}}$ is the Pauli matrix vector. The interlayer moiré potential takes the same form as that in TBG [1,5], namely,

$$T(\mathbf{r}) = \sum_{j=1}^{3} T_{\mathbf{q}_j} e^{i\mathbf{q}_j\cdot\mathbf{r}}, \qquad \mathbf{q}_j = R_{\zeta_j}(\mathbf{K}_- - \mathbf{K}_+),$$
$$T_{\mathbf{q}_j} = w_0\sigma_0 + w_1(\sigma_x\cos\zeta_j + \sigma_y\sin\zeta_j). \tag{3}$$

Here, $\zeta_j = (2\pi/3)(j-1)$, R_ζ is the rotation matrix of angle ζ, and w_0 and w_1 are the interlayer hoppings at AA and AB stacking positions, respectively. The $\mathbf{q}_j$ vectors are illustrated in Fig. 1(c). We have neglected the $-l\theta/2$ rotations of the Dirac Hamiltonians in Eq. (1), which is a valid approximation for small θ [1,5]. When $E_\Delta = 0$ and $a_+ = a_-$, H has a particle-hole symmetry $\mathcal{P}H\mathcal{P}^{-1} = -H$, where $\mathcal{P}$ is given by

$$\mathcal{P}|\mathbf{r}, l, \eta, \alpha\rangle = \eta l|\mathcal{R}_{\hat{\mathbf{x}}}\mathbf{r}, l, \eta, -\alpha\rangle, \tag{4}$$

and where $\mathcal{R}_{\hat{\mathbf{x}}}$ is the reflection matrix for the yz plane. As discussed in Supplemental Material [39] Sec. I, this is different from but related to the particle-hole transformation

previously discussed for TBG [4,5]. Note that when $m_+ = m_- = E_\Delta = 0$, $v_+ = v_-$, and $a_+ = a_-$, Eq. (1) reduces to the two-valley model for TBG.

To a good approximation, one can neglect any changes of parameters in Kekulé-O graphene compared to normal graphene except for the Dirac mass m_l. We take $a_\pm = a_{\mathrm{Gr}} = 0.246$ nm and $v_\pm = v_{\mathrm{Gr}}$ where $\hbar v_{\mathrm{Gr}}/a_{\mathrm{Gr}} = 2.5$ eV, so that the interlayer biaxial strain $\epsilon = 0$. We use $w_1 = 110$ meV and $w_0/w_1 = 0.8$, which are typical parameters for TBG near $\theta = 1°$ [1,42]. Additionally, we take $E_\Delta = 0$ for simplicity. Results with different parameter choices including various values of w_0/w_1 and nonzero values of E_Δ and ϵ are given in Supplemental Material [39] Sec. IV. Note that the sign of each Dirac mass m_l in Eq. (1) can be flipped by applying a unitary change of basis. As a result, we take $m_l \geq 0$ without loss of generality.

TGKG.—We first consider the TGKG system illustrated in Fig. 1(b), in which the top layer is Kekulé-O graphene with $m_+ \geq 0$ and the bottom layer is normal graphene with $m_- = 0$. In this case, the Hamiltonian commutes with the translation operators

$$T_{\mathbf{R}}|\mathbf{r}, l, \eta, \alpha\rangle = e^{i(\mathbf{q}_1\cdot\mathbf{R})\eta(l-1)/2}|\mathbf{r}+\mathbf{R}, l, \eta, \alpha\rangle \qquad (5)$$

for $\mathbf{R}$ in the moiré superlattice L_M, which is defined as the reciprocal of the Bravais lattice P_M generated by $\mathbf{q}_1 - \mathbf{q}_2$ and $\mathbf{q}_1 - \mathbf{q}_3$. As a result, TGKG has the same moiré unit cell as TBG. The moiré BZ of TGKG is the larger hexagon BZ_M in Fig. 1(d).

TGKG generally has magnetic space group $P61'$ (No. 168.110 in the BNS setting [43]) generated by $T_{\mathbf{R}}$ for $\mathbf{R} \in L_M$, C_{6z} (rotation by $\pi/3$ about $\hat{\mathbf{z}}$), and $\mathcal{T}$ (antiunitary spinless time reversal). These operators are given in Supplemental Material [39] Table S1.

Figure 2(a) shows the band structure of TGKG with $\theta = 0.7°$ and $m_+ = 100$ meV. We use band index $n \neq 0$ to denote the $|n|$th conduction (valence) band for $n > 0$ ($n < 0$). The four connected bands $-2 \leq n \leq 2$ around charge neutrality (shown in red) are isolated from higher bands, and the two bands $n = \pm 2$ are extremely flat. Using magnetic topological quantum chemistry (MTQC) [44–46], we find that these four bands are consistent with elementary band corepresentation (EBCR) $({}^1E^2E)_{2b}$ of $P61'$. A full table of EBCRs for each magnetic space group can be found on the Bilbao Crystallographic Server [17,46]. EBCR $({}^1E^2E)_{2b}$ corresponds to a system with two orbitals per site on a honeycomb lattice L_{hc}. These four bands can be approximately described by the honeycomb lattice tight-binding model

$$H_{\mathrm{hc}} = \sum_{\ell,\ell'=\pm 1} t_{\ell\cdot\ell'} \sum_{\langle j,j'\rangle \in L_{\mathrm{hc}}} e^{i(\ell-\ell')\varphi_{j'j}}|j', \ell'\rangle\langle j, \ell|. \qquad (6)$$

Here, t_+ and t_- are real hopping parameters, $|j, \ell\rangle$ is an orbital with angular momentum ℓ modulo 3 on site j, $\langle j, j'\rangle$ runs over all nearest neighbors in L_{hc}, and $\varphi_{j'j}$ is the angle from an arbitrary fixed axis to the ray from site j to site j'. When $|t_+| = |t_-|$, the highest and lowest bands of this model are exactly flat [24,25,28]. See Supplemental Material [39] Sec. III for a construction of the compact localized states and noncontractible loop states for the flat bands in this case [47].

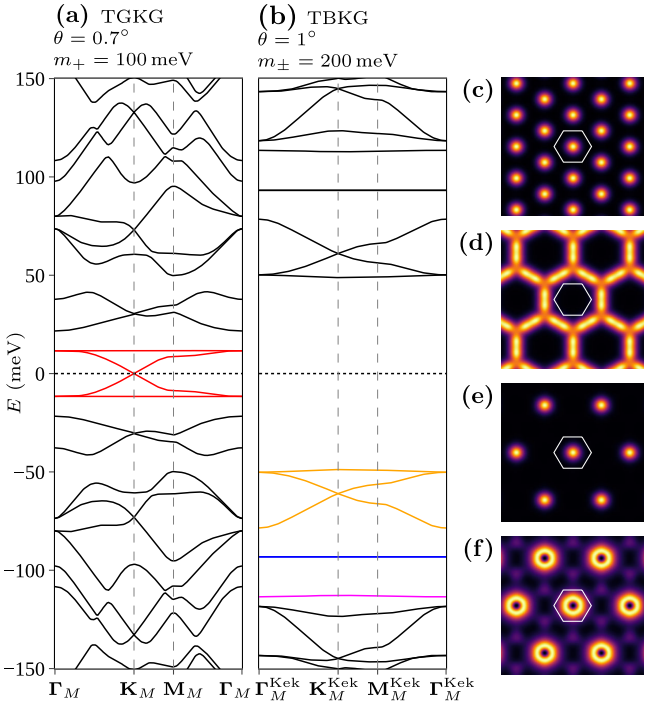

FIG. 2. (a) Band structure of TGKG with the magic parameters $\theta = 0.7°$ and $m_+ = 100$ meV. Bands $-2 \leq n \leq 2$ (shown in red) have the symmetries of a two-orbital honeycomb lattice model. (b) Band structure of TBKG with $\theta = 1°$ and $m_\pm = 200$ meV. Bands $-3 \leq n \leq -1$ (shown in orange), $-5 \leq n \leq -4$ (shown in blue), and $n = -6$ (shown in magenta) have the symmetries of one-orbital kagome lattice, two-orbital triangular lattice, and one-orbital triangular lattice models, respectively. The dashed black lines indicate the Fermi level at charge neutrality, which must be 0 because of the particle-hole symmetry in Eq. (4). (c)–(f) The total charge density of the bands shown in red [in panel (a)], orange, blue, and magenta [in panel (b)], respectively. In each plot, the white hexagon is a unit cell for the moiré superlattice L_M of TGKG. Note that (d)–(f) which are plots for TBKG show periodicity with respect to a $\sqrt{3} \times \sqrt{3}$ enlarged superlattice.

Although the Wannier orbitals for bands $-2 \leq n \leq 2$ must form a honeycomb lattice, their total charge density, shown in Fig. 2(c), is peaked on the triangular lattice formed by the AA stacking positions. A similar phenomenon occurs in magic angle TBG, in which case it is known that each Wannier orbital has a three-lobed "fidget spinner" shape [48–50].

Figure 3(a) shows the bandwidth of the $n = \pm 2$ two-orbital honeycomb lattice flat bands as a function of θ and m_+. We observe two stripes in the parameter space in which the bandwidth reduces to approximately 1 meV.

In particular, bandwidth minima are achieved in two regimes: near $\theta = 1°$, $m_+ = 0$, which is the magic angle TBG regime, and near $\theta = 0.7°$, $m_+ = 100$ meV, which we call the magic TGKG regime and illustrate in Fig. 2(a). The experimentally measured Dirac masses are approximately 200 meV with lithium intercalation [32] and 100 meV with dilute lithium deposition [34]. Therefore, the magic TGKG regime for honeycomb lattice flat bands is experimentally realistic.

TBKG.—We now consider the TBKG system illustrated in Fig. 1(b), in which both layers are Kekulé-O graphene. For simplicity, we assume equal Dirac masses $m_+ = m_- \geq 0$. When both $m_\pm$ are nonzero, the Hamiltonian only commutes with the translation operators $T_{\mathbf{R}}$ in Eq. (5) for $\mathbf{R}$ in the Kekulé moiré superlattice L_M^{Kek}, which is defined as the reciprocal of the Bravais lattice P_M^{Kek} generated by $\mathbf{q}_1$ and $\mathbf{q}_2$. L_M^{Kek} is a $\sqrt{3} \times \sqrt{3}$ superlattice of L_M and the Kekulé moire BZ is the smaller hexagon $\mathrm{BZ}_M^{\mathrm{Kek}}$ in Fig. 1(d).

TBKG generally has magnetic space group $P61'$ just like TGKG. In the special case considered here in which $m_+ = m_-$ and $E_\Delta = 0$, the magnetic space group expands to $P6221'$ (No. 177.150 in the BNS setting [43]) because of the C_{2x} (rotation by π about the $\hat{\mathbf{x}}$) symmetry generator. However, we will use $P61'$ to emphasize that our results are stable against small C_{2x} symmetry breaking perturbations. The $P61'$ symmetry operators are given in Supplemental Material [39] Table S1.

Figure 2(b) shows the band structure of TBKG with $\theta = 1°$ and $m_\pm = 200$ meV. There are 12 low energy bands, which result from folding the four low energy bands of TBG into $\mathrm{BZ}_M^{\mathrm{Kek}}$ and then adding the Dirac masses $m_\pm$. The six valence bands form three groups of connected bands. Using MTQC, we identify bands $-3 \leq n \leq -1$ (shown in orange), $-5 \leq n \leq -4$ (shown in blue), and $n = -6$ (shown in magenta) with EBCRs $(B)_{3c}$, $({}^1E_2{}^2E_2)_{1a}$, and $(A)_{1a}$ of $P61'$, respectively. The conduction bands are related to the valence bands by the particle-hole transformation $\mathcal{P}$ in Eq. (4) and their EBCRs are given in Supplemental Material [39] Table S1. It is evident that bands $n = \pm 1, \pm 4, \pm 5, \pm 6$ are extremely flat.

We now consider the three groups of valence bands separately. First, EBCR $(B)_{3c}$ corresponds to a system with a single orbital per site on a kagome lattice L_{kag}. Accordingly, bands $-3 \leq n \leq -1$ can be approximately described by the kagome lattice tight-binding model

$$H_{\mathrm{kag}} = t \sum_{\langle j,j' \rangle \in L_{\mathrm{kag}}} |j'\rangle\langle j|, \tag{7}$$

where t is a real hopping parameter, $|j\rangle$ is the orbital on site j, and $\langle j, j' \rangle$ runs over all nearest neighbors in L_{kag}. This Hamiltonian always has an exactly flat band [24,26,28] composed of compact localized states and noncontractible loop states [47], as explained in Supplemental Material [39] Sec. III. Figure 2(d) shows the total charge density of bands $-3 \leq n \leq -1$, which is peaked at kagome lattice sites.

Next, EBCR $({}^1E_2{}^2E_2)_{1a}$ corresponds to a system with two orbitals per site on a triangular lattice L_{tri}. Therefore, bands $-5 \leq n \leq -4$ can be approximately described by the triangular lattice tight-binding model

$$H_{\mathrm{tri\text{-}2}} = \sum_{\ell,\ell'=\pm 1} t_{\ell\cdot\ell'} \sum_{\langle j,j' \rangle \in L_{\mathrm{tri}}} e^{i(\ell-\ell')\varphi_{j',j}} |j',\ell'\rangle\langle j,\ell|. \tag{8}$$

The parameters and notations here are identical to those in Eq. (6) except that the sites j here form a triangular lattice. Figure 2(e) shows the total charge density of bands $-5 \leq n \leq -4$, which is peaked at triangular lattice sites.

Finally, EBCR $(A)_{1a}$ corresponds to a system with a single orbital per site on a triangular lattice L_{tri}. As a result, band $n = -6$ can be approximately described by the triangular lattice tight-binding model

$$H_{\mathrm{tri\text{-}1}} = t \sum_{\langle j,j' \rangle \in L_{\mathrm{tri}}} |j'\rangle\langle j|. \tag{9}$$

The parameters and notations here are identical to those in Eq. (7) except that the sites j here form a triangular lattice. Figure 2(f) shows the total charge density of band $n = -6$, which has peaks surrounding triangular lattice sites.

Figures 3(b)–3(d) show the bandwidths of the $n = \pm 1$ one-orbital kagome lattice, $-5 \leq n \leq -4$ or $4 \leq n \leq 5$ two-orbital triangular lattice, and $n = \pm 6$ one-orbital triangular lattice flat bands, respectively, as a function of θ and $m_\pm$.

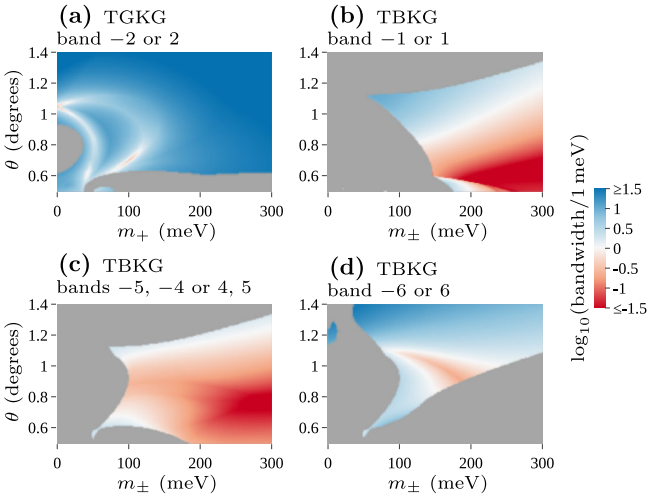

FIG. 3. (a) The bandwidth of band $n = \pm 2$ for TGKG as a function of θ and m_+. (b)–(d) The bandwidth of band $n = \pm 1$, bands $-5 \leq n \leq -4$ or $4 \leq n \leq 5$, and band $n = \pm 6$ for TBKG, respectively, as a function of θ and $m_\pm$. In (a)–(d) the nongray regions show parameters for which MTQC analysis indicates EBCR $({}^1E^2E)_{2b}$, $(B)_{3c}$, $({}^1E_2{}^2E_2)_{1a}$, and $(A)_{1a}$ of $P61'$ for TGKG bands $-2 \leq n \leq 2$, TBKG bands $-3 \leq n \leq -1$, TBKG bands $-5 \leq n \leq -4$, and TBKG band $n = -6$, respectively.

The one-orbital kagome lattice and two-orbital triangular lattice bandwidths generally decrease with increasing $m_{\pm}$ and decreasing θ. One the other hand, the one-orbital triangular lattice bandwidth is smallest for $0.8° \lesssim \theta \lesssim 1.1°$ and $100\ \text{meV} \lesssim m_{\pm} \lesssim 200\ \text{meV}$. The Dirac masses required to realize kagome lattice and triangular lattice flat bands in TBKG are thus experimentally realistic.

Discussion.—We have shown that for twist angles near $\theta = 1°$ and Dirac masses m_l within an experimentally realistic range, TGKG exhibits a two-orbital honeycomb lattice flat band model at charge neutrality, while TBKG exhibits both kagome and triangular lattice flat band models at low energies which are quite robust against parameter variation. When interactions are included, the nontrivial flat bands of the honeycomb and kagome lattice models become promising highly tunable platforms for the realization of strongly correlated phases such as Mott insulators, charge or spin density waves, and spin liquids [51,52]. We leave for future work the possibility of inducing spin-orbit coupling or magnetism through substrate coupling or other means. These effects generically produce flat (spin) Chern bands [28], in which fractional Chern or topological insulators may be realized [53].

For TGKG, when the Dirac mass is large ($m_{+} \gtrsim 500$ meV), the Kekulé-O graphene layer has a sufficiently large gap to allow a perturbative treatment. As explained in [28], an effective moiré model can be derived for the non-Kekulé layer, in which the two valleys are coupled by a moiré potential. However, this perturbative model gives qualitatively incorrect band structures for small Dirac masses m_{+}, and in such cases the full model in Eq. (1) is required.

In an ideal realization of TGKG or TBKG, care must be taken to avoid charge transfer from the adatoms inducing Kekulé-O order into the graphene layers, since the flat bands are near the charge neutrality point of pristine graphene. In Ref. [34] the authors used a dilute concentration of lithium adatoms with negligible charge transfer to the graphene layer, and observed a well-resolved Kekulé-O order despite the disordered adatom arrangement [33]. Charge transfer may also be avoided through intercalation or deposition of both donor and acceptor atoms, for instance, hydrogen and lithium atoms which hole-dope and electron-dope graphene, respectively [32,34]. First-principles calculations and experimental studies are needed to address these issues.

We thank Ali Yazdani, Christopher Gutiérrez, Changhua Bao, Jonah Herzog-Arbeitman, and Yves H. Kwan for valuable discussions. This work is supported by the Alfred P. Sloan Foundation, the National Science Foundation through Princeton University's Materials Research Science and Engineering Center DMR-2011750, and the National Science Foundation under award No. DMR-2141966. Additional support is provided by the Gordon and Betty Moore Foundation through Grant No. GBMF8685 towards the Princeton theory program.

[1] R. Bistritzer and A. H. MacDonald, Moiré bands in twisted double-layer graphene, Proc. Natl. Acad. Sci. U.S.A. **108**, 12233 (2011).
[2] H. C. Po, L. Zou, T. Senthil, and A. Vishwanath, Faithful tight-binding models and fragile topology of magic-angle bilayer graphene, Phys. Rev. B **99**, 195455 (2019).
[3] J. Ahn, S. Park, and B. J. Yang, Failure of Nielsen-Ninomiya theorem and fragile topology in two-dimensional systems with space-time inversion symmetry: Application to twisted bilayer graphene at magic angle, Phys. Rev. X **9**, 021013 (2019).
[4] Z. Song, Z. Wang, W. Shi, G. Li, C. Fang, and B. A. Bernevig, All magic angles in twisted bilayer graphene are topological, Phys. Rev. Lett. **123**, 036401 (2019).
[5] Z.-D. Song, B. Lian, N. Regnault, and B. A. Bernevig, Twisted bilayer graphene. II. Stable symmetry anomaly, Phys. Rev. B **103**, 205412 (2021).
[6] Y. Cao, V. Fatemi, S. Fang, K. Watanabe, T. Taniguchi, E. Kaxiras, and P. Jarillo-Herrero, Unconventional superconductivity in magic-angle graphene superlattices, Nature (London) **556**, 43 (2018).
[7] Y. Cao, V. Fatemi, A. Demir, S. Fang, S. L. Tomarken, J. Y. Luo, J. D. Sanchez-Yamagishi, K. Watanabe, T. Taniguchi, E. Kaxiras, R. C. Ashoori, and P. Jarillo-Herrero, Correlated insulator behaviour at half-filling in magic-angle graphene superlattices, Nature (London) **556**, 80 (2018).
[8] M. Yankowitz, S. Chen, H. Polshyn, Y. Zhang, K. Watanabe, T. Taniguchi, D. Graf, A. F. Young, and C. R. Dean, Tuning superconductivity in twisted bilayer graphene, Science **363**, 1059 (2019).
[9] A. L. Sharpe, E. J. Fox, A. W. Barnard, J. Finney, K. Watanabe, T. Taniguchi, M. A. Kastner, and D. Goldhaber-Gordon, Emergent ferromagnetism near three-quarters filling in twisted bilayer graphene, Science **365**, 605 (2019).
[10] X. Lu, P. Stepanov, W. Yang, M. Xie, M. A. Aamir, I. Das, C. Urgell, K. Watanabe, T. Taniguchi, G. Zhang, A. Bachtold, A. H. MacDonald, and D. K. Efetov, Superconductors, orbital magnets and correlated states in magic-angle bilayer graphene, Nature (London) **574**, 653 (2019).
[11] M. Serlin, C. L. Tschirhart, H. Polshyn, Y. Zhang, J. Zhu, K. Watanabe, T. Taniguchi, L. Balents, and A. F. Young, Intrinsic quantized anomalous Hall effect in a moiré heterostructure, Science **367**, 900 (2020).
[12] K. P. Nuckolls, M. Oh, D. Wong, B. Lian, K. Watanabe, T. Taniguchi, B. A. Bernevig, and A. Yazdani, Strongly correlated Chern insulators in magic-angle twisted bilayer graphene, Nature (London) **588**, 610 (2020).
[13] Y. Xie, A. T. Pierce, J. M. Park, D. E. Parker, E. Khalaf, P. Ledwith, Y. Cao, S. H. Lee, S. Chen, P. R. Forrester, K. Watanabe, T. Taniguchi, A. Vishwanath, P. Jarillo-Herrero, and A. Yacoby, Fractional Chern insulators in magic-angle twisted bilayer graphene, Nature (London) **600**, 439 (2021).
[14] G. Chen, A. L. Sharpe, P. Gallagher, I. T. Rosen, E. J. Fox, L. Jiang, B. Lyu, H. Li, K. Watanabe, T. Taniguchi, J. Jung, Z. Shi, D. Goldhaber-Gordon, Y. Zhang, and F. Wang, Signatures of tunable superconductivity in a trilayer graphene moiré superlattice, Nature (London) **572**, 215 (2019).

[15] J. M. Park, Y. Cao, K. Watanabe, T. Taniguchi, and P. Jarillo-Herrero, Tunable strongly coupled superconductivity in magic-angle twisted trilayer graphene, Nature (London) **590**, 249 (2021).

[16] Z. Hao, A. M. Zimmerman, P. Ledwith, E. Khalaf, D. H. Najafabadi, K. Watanabe, T. Taniguchi, A. Vishwanath, and P. Kim, Electric field–tunable superconductivity in alternating-twist magic-angle trilayer graphene, Science **371**, 1133 (2021).

[17] Y. Xu, S. Liu, D. A. Rhodes, K. Watanabe, T. Taniguchi, J. Hone, V. Elser, K. F. Mak, and J. Shan, Correlated insulating states at fractional fillings of moiré superlattices, Nature (London) **587**, 214 (2020).

[18] Z. Zhang, Y. Wang, K. Watanabe, T. Taniguchi, K. Ueno, E. Tutuc, and B. J. LeRoy, Flat bands in twisted bilayer transition metal dichalcogenides, Nat. Phys. **16**, 1093 (2020).

[19] B. A. Foutty, C. R. Kometter, T. Devakul, A. P. Reddy, K. Watanabe, T. Taniguchi, L. Fu, and B. E. Feldman, Mapping twist-tuned multi-band topology in bilayer WSe_2, arXiv:2304.09808.

[20] J. Cai, E. Anderson, C. Wang, X. Zhang, X. Liu, W. Holtzmann, Y. Zhang, F. Fan, T. Taniguchi, K. Watanabe, Y. Ran, T. Cao, L. Fu, D. Xiao, W. Yao, and X. Xu, Signatures of fractional quantum anomalous Hall states in twisted $MoTe_2$ bilayer, Nature (London) **622**, 63 (2023).

[21] Y. Zeng, Z. Xia, K. Kang, J. Zhu, P. Knüppel, C. Vaswani, K. Watanabe, T. Taniguchi, K. F. Mak, and J. Shan, Integer and fractional Chern insulators in twisted bilayer $MoTe_2$, arXiv:2305.00973.

[22] E. H. Lieb, Two theorems on the Hubbard model, Phys. Rev. Lett. **62**, 1201 (1989).

[23] A. Mielke, Ferromagnetic ground states for the Hubbard model on line graphs, J. Phys. A **24**, L73 (1991).

[24] D. Călugăru, A. Chew, L. Elcoro, Y. Xu, N. Regnault, Z. D. Song, and B. A. Bernevig, General construction and topological classification of crystalline flat bands, Nat. Phys. **18**, 185 (2022).

[25] C. Wu, D. Bergman, L. Balents, and S. Das Sarma, Flat bands and Wigner crystallization in the honeycomb optical lattice, Phys. Rev. Lett. **99**, 070401 (2007).

[26] D. L. Bergman, C. Wu, and L. Balents, Band touching from real-space topology in frustrated hopping models, Phys. Rev. B **78**, 125104 (2008).

[27] M. G. Scheer, K. Gu, and B. Lian, Magic angles in twisted bilayer graphene near commensuration: Towards a hyper-magic regime, Phys. Rev. B **106**, 115418 (2022).

[28] M. G. Scheer and B. Lian, Kagome and honeycomb flat bands in moiré graphene, Phys. Rev. B **108**, 245136 (2023).

[29] C. Gutiérrez, C. J. Kim, L. Brown, T. Schiros, D. Nordlund, E. B. Lochocki, K. M. Shen, J. Park, and A. N. Pasupathy, Imaging chiral symmetry breaking from Kekulé bond order in graphene, Nat. Phys. **12**, 950 (2016).

[30] K. Sugawara, K. Kanetani, T. Sato, and T. Takahashi, Fabrication of Li-intercalated bilayer graphene, AIP Adv. **1**, 022103 (2011).

[31] K. Kanetani, K. Sugawara, T. Sato, R. Shimizu, K. Iwaya, T. Hitosugi, and T. Takahashi, Ca intercalated bilayer graphene as a thinnest limit of superconducting C_6Ca, Proc. Natl. Acad. Sci. U.S.A. **109**, 19610 (2012).

[32] C. Bao, H. Zhang, T. Zhang, X. Wu, L. Luo, S. Zhou, Q. Li, Y. Hou, W. Yao, L. Liu, P. Yu, J. Li, W. Duan, H. Yao, Y. Wang, and S. Zhou, Experimental evidence of chiral symmetry breaking in Kekulé-ordered graphene, Phys. Rev. Lett. **126**, 206804 (2021).

[33] V. V. Cheianov, V. I. Fal'ko, O. Syljuåsen, and B. L. Altshuler, Hidden Kekulé ordering of adatoms on graphene, Solid State Commun. **149**, 1499 (2009).

[34] A. C. Qu, P. Nigge, S. Link, G. Levy, M. Michiardi, P. L. Spandar, T. Matthé, M. Schneider, S. Zhdanovich, U. Starke, C. Gutiérrez, and A. Damascelli, Ubiquitous defect-induced density wave instability in monolayer graphene, Sci. Adv. **8**, 1 (2022).

[35] S. Y. Li, Y. Zhang, L. J. Yin, and L. He, Scanning tunneling microscope study of quantum Hall isospin ferromagnetic states in the zero Landau level in a graphene monolayer, Phys. Rev. B **100**, 085437 (2019).

[36] X. Liu, G. Farahi, C. L. Chiu, Z. Papic, K. Watanabe, T. Taniguchi, M. P. Zaletel, and A. Yazdani, Visualizing broken symmetry and topological defects in a quantum Hall ferromagnet, Science **375**, 321 (2022).

[37] K. P. Nuckolls, R. L. Lee, M. Oh, D. Wong, T. Soejima, J. P. Hong, D. Călugăru, J. Herzog-Arbeitman, B. A. Bernevig, K. Watanabe, T. Taniguchi, N. Regnault, M. P. Zaletel, and A. Yazdani, Quantum textures of the many-body wavefunctions in magic-angle graphene, Nature (London) **620**, 525 (2023).

[38] O. V. Gamayun, V. P. Ostroukh, N. V. Gnezdilov, I. Adagideli, and C. W. Beenakker, Valley-momentum locking in a graphene superlattice with Y-shaped Kekulé bond texture, New J. Phys. **20**, 023016 (2018).

[39] See Supplemental Material at http://link.aps.org/supplemental/10.1103/PhysRevLett.131.266501, which includes Refs. [40,41], for information about symmetry operators, Kekulé-O graphene, compact localized states and noncontractible loop states, and parameter variation.

[40] Y. Xu, L. Elcoro, Z. D. Song, B. J. Wieder, M. G. Vergniory, N. Regnault, Y. Chen, C. Felser, and B. A. Bernevig, High-throughput calculations of magnetic topological materials, Nature (London) **586**, 702 (2020).

[41] Z. Wang, S. M. Selbach, and T. Grande, Van der Waals density functional study of the energetics of alkali metal intercalation in graphite, RSC Adv. **4**, 4069 (2014).

[42] S. Carr, S. Fang, Z. Zhu, and E. Kaxiras, Exact continuum model for low-energy electronic states of twisted bilayer graphene, Phys. Rev. Res. **1**, 013001 (2019).

[43] S. V. Gallego, E. S. Tasci, G. de la Flor, J. M. Perez-Mato, and M. I. Aroyo, Magnetic symmetry in the Bilbao Crystallographic Server: A computer program to provide systematic absences of magnetic neutron diffraction, J. Appl. Crystallogr. **45**, 1236 (2012).

[44] B. Bradlyn, L. Elcoro, J. Cano, M. G. Vergniory, Z. Wang, C. Felser, M. I. Aroyo, and B. A. Bernevig, Topological quantum chemistry, Nature (London) **547**, 298 (2017).

[45] J. Kruthoff, J. De Boer, J. Van Wezel, C. L. Kane, and R. J. Slager, Topological classification of crystalline insulators through band structure combinatorics, Phys. Rev. X **7**, 041609 (2017).

[46] L. Elcoro, B. J. Wieder, Z. Song, Y. Xu, B. Bradlyn, and B. A. Bernevig, Magnetic topological quantum chemistry, Nat. Commun. **12**, 4 (2021).

[47] J. W. Rhim and B. J. Yang, Classification of flat bands according to the band-crossing singularity of Bloch wave functions, Phys. Rev. B **99**, 045107 (2019).

[48] M. Koshino, N. F. Yuan, T. Koretsune, M. Ochi, K. Kuroki, and L. Fu, Maximally localized Wannier orbitals and the extended Hubbard model for twisted bilayer graphene, Phys. Rev. X **8**, 031087 (2018).

[49] J. Kang and O. Vafek, Symmetry, maximally localized Wannier states, and a low-energy model for twisted bilayer graphene narrow bands, Phys. Rev. X **8**, 031088 (2018).

[50] H. C. Po, L. Zou, A. Vishwanath, and T. Senthil, Origin of Mott insulating behavior and superconductivity in twisted bilayer graphene, Phys. Rev. X **8**, 031089 (2018).

[51] S. Yan, D. A. Huse, and S. R. White, Spin-liquid ground state of the $S = 1/2$ kagome Heisenberg antiferromagnet, Science **332**, 1173 (2011).

[52] J. X. Yin, B. Lian, and M. Z. Hasan, Topological kagome magnets and superconductors, Nature (London) **612**, 647 (2022).

[53] E. Tang, J. W. Mei, and X. G. Wen, High-temperature fractional quantum Hall states, Phys. Rev. Lett. **106**, 236802 (2011).